

Stability of steep gravity–capillary solitary waves in deep water

By DAVID C. CALVO AND T. R. AKYLAS

Department of Mechanical Engineering, Massachusetts Institute of Technology,
Cambridge, MA 02139, USA

(Received 10 June 2000 and in revised form 2 July 2001)

The stability of steep gravity–capillary solitary waves in deep water is numerically investigated using the full nonlinear water-wave equations with surface tension. Out of the two solution branches that bifurcate at the minimum gravity–capillary phase speed, solitary waves of depression are found to be stable both in the small-amplitude limit when they are in the form of wavepackets and at finite steepness when they consist of a single trough, consistent with observations. The elevation-wave solution branch, on the other hand, is unstable close to the bifurcation point but becomes stable at finite steepness as a limit point is passed and the wave profile features two well-separated troughs. Motivated by the experiments of Longuet-Higgins & Zhang (1997), we also consider the forced problem of a localized pressure distribution applied to the free surface of a stream with speed below the minimum gravity–capillary phase speed. We find that the finite-amplitude forced solitary-wave solution branch computed by Vanden-Broeck & Dias (1992) is unstable but the branch corresponding to Rayleigh's linearized solution is stable, in agreement also with a weakly nonlinear analysis based on a forced nonlinear Schrödinger equation. The significance of viscous effects is assessed using the approach proposed by Longuet-Higgins (1997): while for free elevation waves the instability predicted on the basis of potential-flow theory is relatively weak compared with viscous damping, the opposite turns out to be the case in the forced problem when the forcing is strong. In this régime, which is relevant to the experiments of Longuet-Higgins & Zhang (1997), the effects of instability can easily dominate viscous effects, and the results of the stability analysis are used to propose a theoretical explanation for the persistent unsteadiness of the forced wave profiles observed in the experiments.

1. Introduction

Short-scale water-wave phenomena, for which surface-tension effects are important, have been actively studied in recent literature. Considerable attention has been paid, in particular, to parasitic capillary wavetrains riding on steep gravity waves (see, for example, Fedorov & Melville 1998; Longuet-Higgins 1995; Perlin, Lin & Ting 1993) and to a new type of gravity–capillary solitary wave brought out in laboratory experiments and field observations (Zhang 1995, 1999). These solitary waves consist of a single trough and, unlike solitary waves of the Korteweg–de Vries (KdV) type, can propagate on deep water, in agreement with theoretical profiles first computed by Longuet-Higgins (1989). While forcing by wind was involved in the original observations, Longuet-Higgins & Zhang (1997) were able to excite such depression solitary waves on deep water more directly by applying a localized pressure distribution to

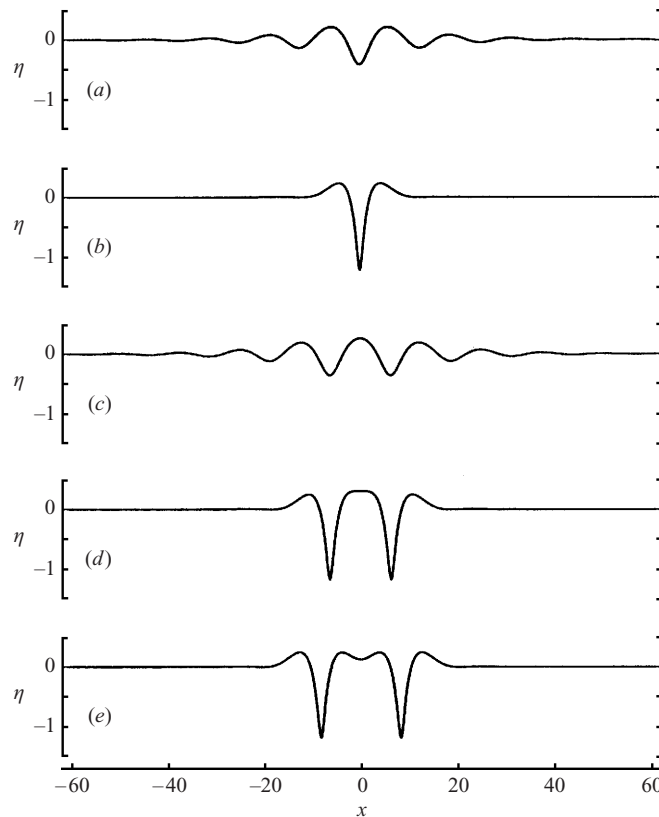


FIGURE 1. Representative free-surface profiles of gravity–capillary solitary waves in deep water. Depression waves are shown in (a) and (b) with speed parameters $\alpha = 0.257$ and $\alpha = 0.4$, respectively; elevation waves are shown in (c), (d) and (e) for $\alpha = 0.257$, $\alpha = 0.38$ (upper branch) and $\alpha = 0.38$ (lower branch), respectively.

a stream moving below the minimum phase speed of infinitesimal gravity–capillary waves; once excitation was removed, a free depression wave propagated with speed and profile consistent with theory taking into account viscous dissipation.

So far, only solitary waves with single-depression profiles have been observed in deep water. Potential-flow theory, on the other hand, suggests a wide variety of other possible solitary-wave solutions. Specifically, the computations of Vanden-Broeck & Dias (1992), apart from depression waves, revealed an elevation-wave solution branch as well. This branch was later studied in detail by Dias, Menasce & Vanden-Broeck (1996) who discovered solitary waves consisting of a series of depression waves by numerically tracing the elevation branch past successive limit points. Representative depression and elevation wave profiles for certain values of the speed parameter $\alpha = gT/\rho c^4$ are displayed in figure 1; here, as in Vanden-Broeck & Dias (1992), dimensionless variables are used throughout with $T/\rho c^2$ as unit length and the wave speed c as unit speed, T being the coefficient of surface tension, ρ the fluid density and g the gravitational acceleration. The elevation and depression solution branches are shown in figure 2 along with the locations on these branches of the particular profiles displayed in figure 1. All solutions have $\alpha > \frac{1}{4}$, implying that wave speeds are less than the minimum phase speed $c_{\min} = (4gT/\rho)^{1/4}$ of infinitesimal gravity–capillary waves.

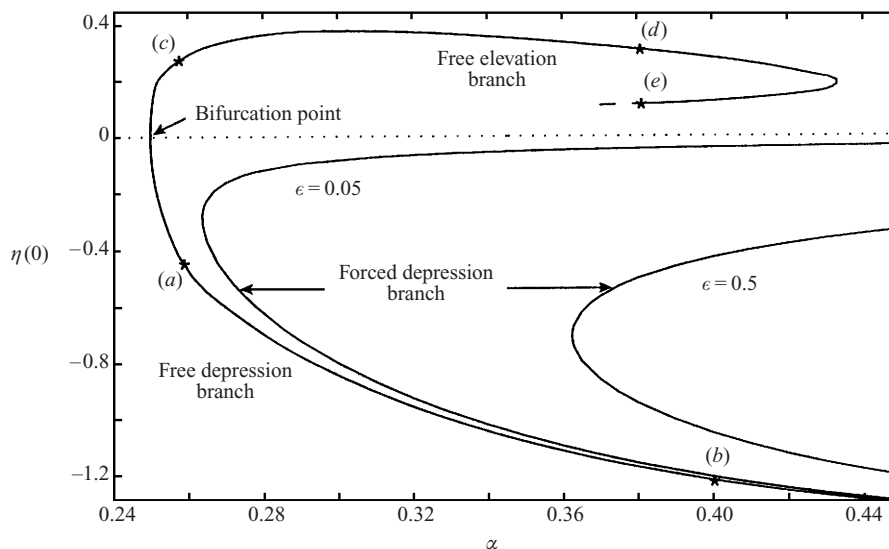


FIGURE 2. Solution diagrams for free and forced deep-water gravity–capillary solitary waves. The free-surface amplitude $\eta(0)$ is plotted against the wave speed parameter $\alpha = gT/\rho c^4$. The dimensionless amplitude of the pressure distribution is $\epsilon = p_{\max}/\rho c^2$, p_{\max} being the pressure peak amplitude.

It is worth noting that depression and elevation waves tend to small-amplitude wavepackets as the solitary-wave speed approaches c_{\min} (see figures 1*a* and 1*c*). Both these wavepacket solutions bifurcate from infinitesimal periodic waves at $\alpha = \frac{1}{4}$ (see figure 2), where the phase speed is equal to the group speed, and may be interpreted as particular envelope-soliton solutions of the nonlinear Schrödinger (NLS) equation such that the carrier oscillations travel at the same speed as their envelope (Akylas 1993; Longuet-Higgins 1993). Motivated by this interpretation, Yang & Akylas (1997) carried out a comprehensive weakly nonlinear analysis of solitary wavepackets in the context of the fifth-order KdV equation—a model equation for small-amplitude gravity–capillary waves in water of finite depth when the Bond number is close to $\frac{1}{3}$. Taking into account the coupling of the carrier oscillations to their envelope, an exponentially small effect beyond all orders of the NLS equation, they pointed out that symmetric elevation and depression solitary wavepackets are the only solution branches that bifurcate at the minimum phase speed; moreover, by allowing for this exponentially small effect, one may explain the origin of the plethora of other types of symmetric and asymmetric solitary waves discussed in related analytical and numerical studies (Buffoni, Champneys & Toland 1995; Zufiria 1987).

The possibility that some of the theoretically predicted gravity–capillary solitary waves, apart from those of depression, could in fact be observed experimentally hinges on their stability properties, but this issue has been addressed thus far in the context of the fifth-order KdV equation only. Calvo (2000), in particular, explored the stability of the two solitary-wave branches that bifurcate at the minimum phase speed by solving the time-dependent fifth-order KdV equation numerically; he came to the conclusion that elevation waves are unstable and evolve to stable depression waves, a somewhat intriguing result given that these two solution types are mirror images of each other in the small-amplitude limit and both are stable according to the NLS equation. It turns out that the instability arises from the coupling of the carrier oscillations to the envelope of solitary wavepackets, an exponentially small

effect that cannot be captured by the NLS theory as remarked earlier; hence, close to the bifurcation point, the instability growth rate of elevation waves is exponentially small with respect to the wave steepness (Calvo, Yang & Akylas 2000). These results are consistent with earlier computations by Malomed & Vanden-Broeck (1996) and the stability analyses of Buryak & Champneys (1997) and Dias & Kuznetsov (1999).

The stability studies cited above are interesting from a theoretical viewpoint but their relevance can be questioned on physical grounds, given the rather limited validity of the fifth-order KdV equation: for the Bond number to be close to $\frac{1}{3}$, the water depth is restricted to a few mm so neglecting viscous dissipation cannot be justified (Zufria 1987). Accordingly, in the present work, having in mind the relatively steep gravity–capillary solitary waves observed experimentally, we shall work with the full deep-water wave equations using numerical techniques. Moreover, while our stability analysis is based on potential-flow theory, we shall make an assessment of viscous effects following the approach proposed by Longuet-Higgins (1997).

The same numerical procedure also proves useful in the stability analysis of forced gravity–capillary solitary waves generated by a localized pressure distribution on the free surface of a stream with speed less than c_{\min} ; this case corresponds directly to the experimental set-up of Longuet-Higgins & Zhang (1997). Steady inviscid solutions to this problem have already been computed by Vanden-Broeck & Dias (1992) who found, in addition to Rayleigh’s linearized solution, a finite-amplitude branch of solutions connected to Rayleigh’s solution branch by a limit point; the geometry of these forced solution branches is shown in figure 2 for blowing on the free surface with two different peak pressure amplitudes.

Out of the two branches of free solitary-wave solutions that bifurcate at the minimum gravity–capillary phase speed, free depression solitary waves are stable both in the small-amplitude limit and at finite steepness, consistent with experimental evidence. Moreover, the stability analysis establishes that wave profiles featuring two well-separated single-depression pulses, which arise when the elevation solution branch is continued past a limit point, are stable as well.

In the forced problem, on the other hand, the finite-amplitude solution branch is found to be always unstable. For relatively strong forcing in particular, the effects of this instability can easily dominate viscous effects, and one would expect the response either to approach Rayleigh’s linearized solution, which is stable, or to remain unsteady when the stream speed is in a range where no stable steady state is available. The latter scenario is relevant to the experiments of Longuet-Higgins & Zhang (1997) and provides an explanation for the persistent unsteadiness of the observed forced wave profiles.

2. Formulation

It is convenient to present the formulation in the context of the forced problem where a stationary localized pressure distribution is applied on the free surface of a fluid stream; the case of a free solitary wave then follows by simply setting the pressure amplitude equal to zero. For computing nonlinear steady solutions to the governing equations, we shall use the boundary-integral-equation method described in Vanden-Broeck & Dias (1992). The stability of these solutions then is tackled following a procedure similar to that devised by Tanaka (1986) for studying the stability of steep gravity solitary waves of the KdV type on water of finite depth, the essential difference being that here we allow for the additional effects of surface tension and forcing.

2.1. Governing equations and steady solutions

In the frame of the pressure distribution, the flow at large depth is a uniform stream moving to the right at constant speed $c < c_{\min}$. The y -axis points upward, $y = 0$ corresponding to the undisturbed level of the free surface. The pressure distribution is taken to be symmetric about $x = 0$, x being the streamwise coordinate. The flow, which is assumed to be incompressible and irrotational, is described by the velocity potential ϕ , and the free-surface elevation is denoted by η .

The governing equations in dimensionless form read

$$\phi_{xx} + \phi_{yy} = 0 \quad (-\infty < x < \infty, -\infty < y < \eta), \quad (2.1)$$

$$\phi_t + \frac{1}{2}(\phi_x^2 + \phi_y^2) + \alpha\eta - \frac{\eta_{xx}}{(1 + \eta_x^2)^{3/2}} + \epsilon p(x) = \frac{1}{2} \quad (y = \eta), \quad (2.2)$$

$$\eta_t + \phi_x \eta_x = \phi_y \quad (y = \eta), \quad (2.3)$$

$$(\phi_x, \phi_y) \rightarrow (1, 0) \quad (\sqrt{x^2 + y^2} \rightarrow \infty), \quad (2.4)$$

where $p(x)$ represents the externally applied pressure. Two dimensionless parameters arise: the speed parameter $\alpha = gT/\rho c^4$, introduced earlier, and $\epsilon = p_{\max}/\rho c^2$ which controls the amplitude of the applied pressure, p_{\max} being the pressure peak amplitude.

For obtaining nonlinear steady solutions of (2.1)–(2.4), it is convenient to use the velocity potential ϕ and stream function ψ , rather than x and y , as independent variables. Specifically, $\psi = 0$ is chosen to define the free-surface streamline and $\phi = 0$ to define the line of symmetry; the fluid region then lies in $\psi < 0$. Moreover, the horizontal (u) and vertical (v) velocity components may be expressed in terms of $f = \phi + i\psi$ and $z = x + iy$ by using the fact that

$$u - iv = \left(\frac{dz}{df} \right)^{-1} = \frac{1}{x_\phi + iy_\phi}. \quad (2.5)$$

The method of solution then is to seek $x_\phi + iy_\phi$ as an analytic function of f in $\psi \leq 0$.

To this end, applying Cauchy's integral theorem to $x_\phi + iy_\phi - 1$ using a path including $\psi = 0$ and a large semicircle that encloses the fluid region, the integrand along the semicircle vanishes on account of (2.4). Setting $\psi = 0$ and taking the real part of the resulting expression then yields the following relation between x_ϕ and $\eta_\phi = y_\phi$:

$$x_\phi = 1 - \frac{1}{\pi} \int_{-\infty}^{\infty} \frac{\eta_\xi}{\xi - \phi} d\xi \quad (\psi = 0), \quad (2.6)$$

the integral being of Cauchy's principal-value form. Furthermore, by considering only symmetric waves and working in the half-domain ($0 \leq \phi < \infty$), (2.6) reduces to

$$x_\phi = 1 - \frac{1}{\pi} \int_0^\infty \eta_\xi \left(\frac{1}{\xi - \phi} + \frac{1}{\xi + \phi} \right) d\xi \quad (\psi = 0). \quad (2.7)$$

The kinematic boundary condition (2.3) is automatically satisfied by the choice of independent variables and, making use of (2.5), the steady version of the dynamic boundary condition (2.2) transforms to

$$\frac{1}{2(x_\phi^2 + \eta_\phi^2)} + \alpha\eta + \frac{\eta_\phi x_{\phi\phi} - x_\phi \eta_{\phi\phi}}{(x_\phi^2 + \eta_\phi^2)^{3/2}} + \epsilon p(\phi) = \frac{1}{2} \quad (\psi = 0); \quad (2.8)$$

the pressure distribution now is a function of the velocity potential on the free-surface

and is taken in the form

$$p(\phi) = \begin{cases} \exp\left(\frac{1}{\phi^2 - 1}\right) & (|\phi| \leq 1) \\ 0 & (|\phi| > 1), \end{cases} \quad (2.9)$$

as in Vanden-Broeck & Dias (1992).

Equations (2.7) and (2.8) define an integro-differential system for η_ϕ and x_ϕ on the free surface; upon solving this system, the free-surface profile $\eta(x)$ is readily determined.

2.2. Linear stability

We denote the steady free-surface elevation, velocity potential and stream function by $H(x)$, $\Phi(x, y)$ and $\Psi(x, y)$, respectively, and consider small disturbances to these quantities:

$$\eta(x, t) = H(x) + \tilde{\eta}(x, t), \quad (2.10)$$

$$\phi(x, y, t) = \Phi(x, y) + \tilde{\phi}(x, y, t), \quad (2.11)$$

$$\psi(x, y, t) = \Psi(x, y) + \tilde{\psi}(x, y, t), \quad (2.12)$$

with $\tilde{\phi}_x = \tilde{\psi}_y$ and $\tilde{\phi}_y = -\tilde{\psi}_x$ so as to satisfy Laplace's equation.

In preparation for the ensuing linear stability analysis, the dynamic condition (2.2) and the kinematic condition (2.3), that apply along the free-surface streamline $y = H + \tilde{\eta}$, are expanded about $y = H$, keeping only terms that are linear in the disturbances. Specifically, the linearized dynamic boundary condition is

$$\begin{aligned} \tilde{\phi}_t + \Phi_x \tilde{\phi}_x + \Phi_y \tilde{\phi}_y + (\Phi_x \Phi_{xy} + \Phi_y \Phi_{yy}) \tilde{\eta} + \alpha \tilde{\eta} + \epsilon p_\phi \Phi_y \tilde{\eta} - \frac{\tilde{\eta}_{xx}}{(1 + H_x^2)^{3/2}} \\ + \frac{3H_{xx}H_x}{(1 + H_x^2)^{5/2}} \tilde{\eta}_x = 0 \quad (y = H), \end{aligned} \quad (2.13)$$

and the linearized kinematic boundary condition is

$$\tilde{\eta}_t + \Phi_x \tilde{\eta}_x + H_x \tilde{\phi}_x + \Phi_{xy} H_x \tilde{\eta} = \tilde{\phi}_y + \Phi_{yy} \tilde{\eta} \quad (y = H). \quad (2.14)$$

It is convenient to use the arclength s of the undisturbed streamline as an independent variable, $s = 0$ being the point of symmetry, and to represent the steady state in terms of the magnitude of the velocity on the free surface, $q = (\Phi_x^2 + \Phi_y^2)^{1/2}$, and the angle the velocity vector makes with the horizontal, $\theta = \arctan(dH/dx)$. Assuming normal-mode perturbations $\propto \exp(\lambda t)$ and making use of $\Phi_x = q \cos \theta$, $dx = ds \cos \theta$, (2.13) then transforms to

$$\lambda \tilde{\phi} = -q \frac{d\tilde{\phi}}{ds} - \left(q \frac{d(q \sin \theta)}{ds} + \alpha \right) \tilde{\eta} + \frac{1}{\cos \theta} \frac{d}{ds} \left(\cos^2 \theta \frac{d\tilde{\eta}}{ds} \right) - \epsilon \frac{dp}{ds} \sin \theta \tilde{\eta}. \quad (2.15)$$

By similar manipulations, (2.14) becomes

$$\lambda \tilde{\eta} = -q \frac{d\tilde{\eta}}{ds} - \frac{1}{\cos \theta} \frac{d\tilde{\psi}}{ds} - \frac{1}{\cos \theta} \frac{d(q \cos \theta)}{ds} \tilde{\eta}. \quad (2.16)$$

Clearly, solutions of the linearized system (2.15) and (2.16) that are bounded and oscillatory as $|\Phi| \rightarrow \infty$ ($\Psi = 0$) correspond to linear waves superposed on a uniform stream at infinity and have neutral stability. If unstable modes exist, therefore, they must decay to zero at infinity. Using this condition, Cauchy's theorem can again be applied to the function $\tilde{\phi} + i\tilde{\psi}$ using the same semicircular contour as before in the

(Φ, Ψ) -plane. After taking the imaginary part of the resulting expression, we find that $\tilde{\phi}$ and $\tilde{\psi}$ form a Hilbert-transform pair:

$$\tilde{\psi} = \frac{1}{\pi} \int_{-\infty}^{\infty} \frac{\tilde{\phi}(s)}{s - \Phi} ds = \mathcal{H}(\tilde{\phi}) \quad (\Psi = 0). \quad (2.17)$$

Making the change $d/ds = qd/d\Phi$, the eigenvalue problem (2.15) and (2.16) then takes the final form

$$\lambda \tilde{\phi} = -q^2 \frac{d\tilde{\phi}}{d\Phi} - \left(q^2 \frac{d(q \sin \theta)}{d\Phi} + \alpha \right) \tilde{\eta} + \frac{q}{\cos \theta} \frac{d}{d\Phi} \left(q \cos^2 \theta \frac{d\tilde{\eta}}{d\Phi} \right) - \epsilon q \frac{dp}{d\Phi} \sin \theta \tilde{\eta}, \quad (2.18)$$

$$\lambda \tilde{\eta} = -q^2 \frac{d\tilde{\eta}}{d\Phi} - \frac{q}{\cos \theta} \frac{d\mathcal{H}(\tilde{\phi})}{d\Phi} - \frac{q}{\cos \theta} \frac{d(q \cos \theta)}{d\Phi} \tilde{\eta}, \quad (2.19)$$

where both $\tilde{\eta}$ and $\tilde{\phi}$ decay to zero as $|\Phi| \rightarrow \infty$. Apart from a difference in normalization scales, this eigenvalue problem agrees with the deep-water limit of the problem solved by Tanaka (1986) if the effects of forcing and surface tension, which contribute the last two terms in (2.18), are neglected. It is noted that if $\theta \rightarrow \frac{1}{2}\pi$, which can occur for steep depression waves when the wave speed is low enough, equations (2.18) and (2.19) become singular and a modified stability analysis is necessary to treat this case. We shall only consider the stability of solitary waves with single-valued surface profiles.

3. Numerical solution

The numerical procedure for computing nonlinear steady wave disturbances is along the same lines as that presented in Vanden-Broeck & Dias (1992) and Dias *et al.* (1996): x_Φ and η_Φ and thereby $\eta(x)$ are determined using finite-difference approximations of equations (2.7) and (2.8). Truncating the domain at a sufficiently large value $\Phi = \Phi_{\max}$, N uniformly spaced mesh points $\Phi_i = (i-1)\Delta\Phi$, $i = 1, \dots, N$, are introduced and the boundary conditions $\eta_\Phi(0) = \eta_\Phi(\Phi_{\max}) = 0$ are imposed.

In the case of depression waves, which can have high curvature in the trough regions, it proved helpful to introduce a non-uniform grid, in terms of a new independent variable γ , via the transformation $\Phi = \beta\gamma + \gamma^m$, where β is a small positive number and m is an odd integer. This transformation is identical to that used by Tanaka (1986) for handling steep solitary gravity waves which have high curvature in the crest regions. In the problem of interest here, when β is small, the transformation stretches out the steep trough region and brings the tails closer to the origin; this proves especially useful, as solitary waves in deep water feature algebraically decaying tails (Akylas, Dias & Grimshaw 1998).

In approximating derivatives and integrals, we followed Tanaka (1986). Specifically, principal-value integrals were computed by first interpolating the integrand at a new set of mesh points, $\tilde{\Phi}_i = (i - \frac{1}{2})\Delta\Phi$, $i = 1, \dots, N$, using the eight-point Lagrangian interpolation formula and then applying the trapezoidal rule; derivatives $d/d\Phi$ and $d/d\gamma$ were approximated using nine-point centred finite-difference formulas.

The discretization of the eigenvalue problem (2.18) and (2.19) was carried out using the same finite-difference approximations and leads to a standard matrix eigenvalue problem. The eigenvalues in fact appear in quartets $[\lambda, -\lambda, \lambda^*, -\lambda^*]$ owing to certain symmetries of the eigenvalue problem; these symmetries can be used to reduce the dimension of the eigenvalue problem, treating λ^2 as the eigenvalue parameter, but, as

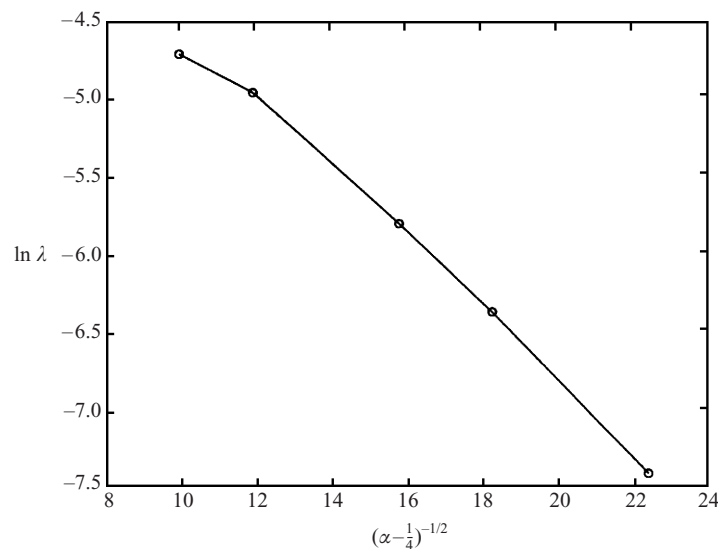


FIGURE 3. Instability growth rates of small-amplitude elevation solitary waves in deep water as the bifurcation point $\alpha = \frac{1}{4}$ is approached.

it turned out, at a great increase in the required resolution, so the eigenvalue problem for λ was solved instead.

The procedure for solving the eigenvalue problem was to first use a moderately fine grid and the QR algorithm to detect possible candidates for eigenvalues; the mode shapes and eigenvalues were then refined using the inverse-power method with shifting. The spectrum, which obeyed the symmetries mentioned above, contains an array of pure imaginary eigenvalues approximating the continuous spectrum of the actual problem. When an instability was present, in addition to these neutral eigenvalues, a pair of pure real eigenvalues was found with eigenvectors decaying to zero at the tails of the solitary wave, as required for eigenfunctions corresponding to unstable modes of the original continuous problem.

A systematic convergence study of numerical solutions for steady solitary-wave profiles was carried out by Dias *et al.* (1996), and our results are in complete agreement with theirs. Examples illustrating the convergence behaviour of eigenvalue computations along with further details of numerical implementation can be found in the Appendix. Care was taken to ensure that the eigenvalues reported below have converged to all the digits displayed.

4. Numerical results

4.1. Free solitary waves

Based on the fifth-order KdV equation, in the small-amplitude limit, elevation solitary waves are unstable with exponentially small growth rates, but depression waves are stable (Calvo *et al.* 2000). We begin by presenting numerical evidence that small-amplitude solitary waves in deep water behave similarly.

To this end, the instability growth rate of elevation waves is plotted in figure 3 on a logarithmic scale against the inverse of the parameter $(\alpha - \frac{1}{4})^{1/2}$. The growth rates begin to fall on a straight line as the bifurcation point is approached ($\alpha \rightarrow \frac{1}{4}$), consistent with the behaviour found using the fifth-order KdV equation. As expected, the wave

α	$\eta(0)$	θ_{\max} (deg.)	Φ_{\max}	$\Delta\Phi$	λ
0.252	0.1820	5.97	200	0.025	0.0006
0.253	0.2077	7.03	150	0.025	0.0017
0.254	0.2275	7.91	150	0.04	0.003
0.257	0.2669	9.90	100	0.04	0.007
0.26	0.2924	11.4	100	0.04	0.009
0.27	0.3411	15.4	85	0.04	0.012
0.28	0.3647	18.6	85	0.04	0.014
0.29	0.3761	21.5	85	0.025	0.0145
0.30	0.3782	24.1	65	0.025	0.0153
0.32	0.3729	28.7	65	0.025	0.0148
0.34	0.3576	32.8	65	0.04	0.014
0.36	0.3477	36.5	65	0.04	0.012
0.38	0.3106	39.8	65	0.025	0.0098
0.40	0.2802	42.9	65	0.025	0.0077

TABLE 1. Instability growth rate λ of free elevation solitary waves for various values of the speed parameter α . The free-surface elevation at the point of symmetry $\eta(0)$, the maximum surface steepness θ_{\max} , and the values of $\Delta\Phi$ and Φ_{\max} used in the computations are listed for reference.

profile spreads out into a wavepacket in this limit so it is computationally difficult to extend the numerical results further. Employing this wavepacket representation, the computed instability mode shape also agrees approximately with the derivative of the solitary-wave profile with respect to the envelope variable, as predicted by the asymptotic theory for the fifth-order KdV equation (Calvo *et al.* 2000). No unstable modes were found for small-amplitude depression waves, in agreement with the fifth-order KdV theory as well.

Away from the bifurcation point, as the elevation-wave steepness increases, the instability growth rate increases as well, attaining a maximum when $\alpha = 0.3$ (see table 1). Beyond this value of α , the growth rate decreases as the limit point at $\alpha = 0.43$ is approached. Near the limit point, instability could be detected but convergence deteriorated so results are presented only up to $\alpha = 0.4$. After the limit point is passed, upon further decreasing α one obtains profiles resembling steep overlapping depression waves, an example of which is shown in figure 1(e). For $\alpha = 0.38$, no instability could be found for this solution type, suggesting that an exchange of stability occurs near the limit point. For the depression solution branch, instabilities could not be found for either small-amplitude or steep solitary waves.

4.2. Forced depression solitary waves

Having in mind the experiments of Longuet-Higgins & Zhang (1997), attention was focused on forced depression solitary waves. We consider both weak ($\epsilon = 0.05$) and strong ($\epsilon = 0.5$) forcing amplitudes corresponding to the response curves shown in figure 2. Starting on the lower-amplitude branch (corresponding to Rayleigh's solution) of each of these curves far from the limit point, no instability can be detected. As the limit point is approached, however, instability sets in as a pair of real eigenvalues, and the onset of this instability occurs closer to the nose of the response curve as the pressure amplitude is decreased. As the limit point is passed and there is a transition to the higher-amplitude branch, the growth rate increases monotonically with α (see table 2). These results were obtained using the values of

$\epsilon = 0.05$				$\epsilon = 0.5$			
α	$\eta(0)$	θ_{\max} (deg.)	λ	α	$\eta(0)$ (deg.)	θ_{\max}	λ
0.279	-0.612	16.1	0.014	0.368	-0.840	25.1	0.059
0.320	-0.928	27.1	0.021	0.447	-1.203	43.3	0.100
0.368	-1.127	36.3	0.027	0.549	-1.343	56.4	0.122
0.447	-1.296	47.9	0.033	0.681	-1.395	68.2	0.133
0.549	-1.386	59.1	0.039				
0.681	-1.416	69.8	0.041				

TABLE 2. Instability growth rates λ for forced depression solitary waves located on the higher-amplitude branches of the response curves in figure 2. The free-surface elevation at the point of symmetry $\eta(0)$ and the maximum surface steepness θ_{\max} are listed for reference. Results were obtained using the numerical parameters $\beta = 0.1$, $m = 3$, $\Phi_{\max} = 132$ ($\gamma_{\max} = 5.1$) and $\Delta\gamma = 7.8 \times 10^{-3}$.

parameters $\beta = 0.1$, $m = 3$, $\Phi_{\max} = 132$ ($\gamma_{\max} = 5.1$) and $\Delta\gamma = 7.8 \times 10^{-3}$; increasing the resolution did not change λ to within the accuracy reported in table 2.

The instability found here is in dramatic contrast with the results for free depression waves discussed earlier: when the surface steepness is large and ϵ is small, in particular, the forced response is essentially a free depression solitary wave profile that is lightly forced; nevertheless, this small amount of forcing is enough to cause instability. Of course, as the pressure amplitude is increased, the instability becomes stronger; for example, in the range of speeds considered here, the growth rates corresponding to $\epsilon = 0.5$ and $\epsilon = 0.05$ differ by a factor of roughly three (see table 2).

These stability results suggest that, under flow conditions for which two steady states are possible, Rayleigh's solution would most likely be attained, the higher-amplitude solution being unstable; on the other hand, the flow presumably would remain unsteady when no stable steady state is available. A detailed description of the dynamics would require a time-dependent simulation of the nonlinear water-wave equations which is beyond the present study. Some insight into the dynamics can be obtained, however, when the pressure amplitude is small and the forced response resembles a small-amplitude wavepacket. As discussed below, the flow then is governed by a forced NLS equation, in terms of which one may explore the evolution of the induced disturbance in this weakly nonlinear régime.

5. Weakly nonlinear forced dynamics

According to linear theory, the steady-state response to a localized pressure disturbance (Rayleigh's solution) becomes unbounded as the current speed approaches c_{\min} owing to a resonance phenomenon (Whitham 1974, §13.9). In the weakly nonlinear régime, when the pressure amplitude is small, this singular behaviour may be resolved by an asymptotic theory. The problem is mathematically similar to the generation of surface waves in a channel by a wavemaker oscillating near a cut-off frequency (Barnard, Mahony & Pritchard 1977), the excitation of acoustic waves in a duct by a piston oscillating near a cut-off frequency (Aranha, Yue & Mei 1982), and the forcing of gravity waves by a moving pressure distribution oscillating at resonant frequency (Akylas 1984). In the latter study, it was found that weakly nonlinear near-resonant flow is governed by a forced NLS equation and, not unexpectedly, this turns out to

be the case here as well. We shall only sketch the main points in the derivation of the forced NLS equation. The steady version of this forced NLS equation was also obtained in recent work by Părău & Dias (2000).

5.1. Forced NLS equation and localized steady solutions

When the forcing amplitude is small ($\epsilon \ll 1$) and the current speed is close to resonant conditions ($\alpha \rightarrow \frac{1}{4}$), the weakly nonlinear response is expected to take the form of a modulated wavepacket with carrier wavenumber k_{\min} corresponding to the minimum gravity–capillary phase speed; in the present non-dimensional formulation, $k_{\min} = \frac{1}{2}$. Moreover, since the phase and group speeds are equal at this wavenumber, the wavepacket envelope is nearly stationary relative to the carrier oscillations.

Accordingly, in terms of the envelope variable $X = \epsilon^{1/2}x$ and the ‘slow’ time variable $\tau = \epsilon t$, the appropriate expansions for the velocity potential and free-surface elevation are

$$\phi(x, y, t) = x + \epsilon^{1/2}\{A(X, \tau)e^{ix/2} + \text{c.c.}\}e^{y/2} + \epsilon\{A_2(X, \tau)e^{ix} + \text{c.c.}\}e^y + \cdots, \quad (5.1)$$

$$\eta(x, t) = \epsilon^{1/2}\{S(X, \tau)e^{ix/2} + \text{c.c.}\} + \epsilon\{S_2(X, \tau)e^{ix} + \text{c.c.}\} + \cdots, \quad (5.2)$$

where $\alpha = \frac{1}{4} + \sigma\epsilon$, $\sigma = O(1)$ being a detuning parameter.

To avoid heavy algebraic details in the derivation of the forced NLS equation, we shall first obtain the forcing and nonlinear terms, ignoring dependence on X ; these terms will then be combined with the familiar linear dispersive term to deduce the complete evolution equation.

Upon substitution of (5.1) and (5.2) into the dynamic and kinematic boundary conditions (2.2) and (2.3), the second-harmonic amplitudes are related to the primary-harmonic amplitudes by

$$S_2 = -S^2, \quad A_2 = -\frac{3}{2}iS^2. \quad (5.3)$$

The equations for the primary harmonic then are

$$iS - A + 2\epsilon(S_\tau + \frac{13}{16}iS^2S^*) = 0, \quad (5.4)$$

$$iA + (1 + 2\sigma\epsilon)S + 2\epsilon(iS_\tau + \frac{15}{32}S^2S^*) = -2\epsilon^{1/2}p(x)e^{-ix/2}. \quad (5.5)$$

Eliminating A from (5.4) and (5.5) and combining the result with the linear dispersive term, as obtained directly from the dispersion relation, yields the forced NLS equation

$$iS_\tau + \frac{1}{2}\sigma S - \frac{1}{2}S_{XX} - \frac{11}{64}S^2S^* = -\pi\hat{p}_m\delta(X), \quad (5.6)$$

where the pressure distribution has been replaced by its limiting form

$$\frac{1}{\epsilon^{1/2}}p\left(\frac{X}{\epsilon^{1/2}}\right)\exp\left(-i\frac{X}{2\epsilon^{1/2}}\right) \longrightarrow 2\pi\hat{p}_m\delta(X), \quad (5.7)$$

and

$$\hat{p}_m = \frac{1}{2\pi} \int_{-\infty}^{\infty} p(x)e^{-ix/2} dx. \quad (5.8)$$

We next look for localized steady solutions of (5.6) for $\sigma > 0$ which correspond to forced finite-amplitude steady flow states for $c < c_{\min}$. To this end, it is convenient to work in the half-domain ($0 < X < \infty$), using the jump condition at $X = 0$ imposed by the delta function in (5.6):

$$S_X = \pi\hat{p}_m \quad (X = 0). \quad (5.9)$$

Following Barnard *et al.* (1977), we write $S(X) = R(X)e^{i\varphi(X)}$ and look for solutions which decay at infinity

$$R \rightarrow 0 \quad (X \rightarrow \infty). \quad (5.10)$$

It is straightforward to show that φ is constant and hence S is real by (5.9), taking $p(x)$ to be symmetric as in (2.9) so \hat{p}_m is real. Moreover, $S(0)$ is given by

$$S(0) = \pm \left\{ \frac{32}{11}\sigma \pm \frac{32}{11}\sigma \left[1 - \frac{11}{16} \left(\frac{\pi\hat{p}_m}{\sigma} \right)^2 \right]^{1/2} \right\}^{1/2}. \quad (5.11)$$

Depending on the sign of $\hat{p}_m S(0)$, two types of responses are possible: when $\hat{p}_m S(0) < 0$, the envelope profile $S(X)$ varies monotonically in $X > 0$ and is given implicitly by

$$X = \sigma^{-1/2} \ln \left(\frac{1 + (1 - 11S^2/64\sigma)^{1/2}}{1 + (1 - 11S(0)^2/64\sigma)^{1/2}} \frac{S(0)}{S} \right) \quad (X > 0); \quad (5.12)$$

this is the small-amplitude analogue of the forced solitary waves discussed earlier, $\hat{p}_m > 0$ and $S(0) < 0$ ($\hat{p}_m < 0$ and $S(0) > 0$) corresponding to blowing (suction) on a depression (elevation) wave. When $\hat{p}_m S(0) > 0$, on the other hand, S attains a local extremum at some $X > 0$. This latter type of response may be interpreted as blowing (suction) on an elevation (depression) wave and was found by Vanden-Broeck & Dias (1992) as well by numerically solving the full water-wave equations.

In both cases noted above, the \pm sign inside the braces in (5.11) implies that two real solution branches exist for $\sigma > \sigma^* = \sqrt{11}\pi\hat{p}_m/4$ which converge to a limit point at $\sigma = \sigma^*$, where the quantity in the brackets vanishes. For the pressure disturbance (2.9), it follows from (5.8) that $\hat{p}_m = 0.0693$ so $\sigma^* = 0.1804$. The response curves found using the forced NLS equation (for $\hat{p}_m S(0) < 0$) are compared in figure 4 with those found numerically using the full water-wave equations as described earlier, for pressure amplitudes $\epsilon = 0.05$ and $\epsilon = 0.015$. Agreement between the limit-point locations clearly improves as ϵ is decreased, but the weakly nonlinear solution rapidly loses accuracy away from the limit point.

5.2. Stability problem

It is most convenient to examine the stability of the localized steady solutions $S = \bar{S}$ over the full domain $-\infty < X < \infty$, using symmetry to extend \bar{S} to $X < 0$. Again, small disturbances in the form of normal modes are assumed by writing $S(X, \tau) = \bar{S}(X) + \{F(X) + iG(X)\} \exp(\hat{\lambda}\tau)$, and upon substituting into (5.8), linearizing, and separating real and imaginary parts, the following system is obtained:

$$\hat{\lambda}F + \frac{1}{2}\sigma G - \frac{1}{2}G_{XX} - \frac{11}{64}\bar{S}^2 G = 0, \quad (5.13)$$

$$\hat{\lambda}G - \frac{1}{2}\sigma F + \frac{1}{2}F_{XX} + \frac{33}{64}\bar{S}^2 F = 0. \quad (5.14)$$

It may be readily shown that for an instability to be possible ($\text{Re}\hat{\lambda} > 0$), both F and G must decay to zero as $|X| \rightarrow \infty$. This eigenvalue problem was solved numerically by discretizing (5.13) and (5.14) using second-order centred finite differences and then using the QR algorithm to find unstable eigenvalues.

Focusing on solutions with $\hat{p}_m S(0) < 0$, Rayleigh's solution branch was again found to be stable. Once σ passes through the critical value σ^* corresponding to the limit point, as transition to the upper solution branch occurs, a pair of real eigenvalues appears, signalling the onset of instability which becomes stronger as σ is further

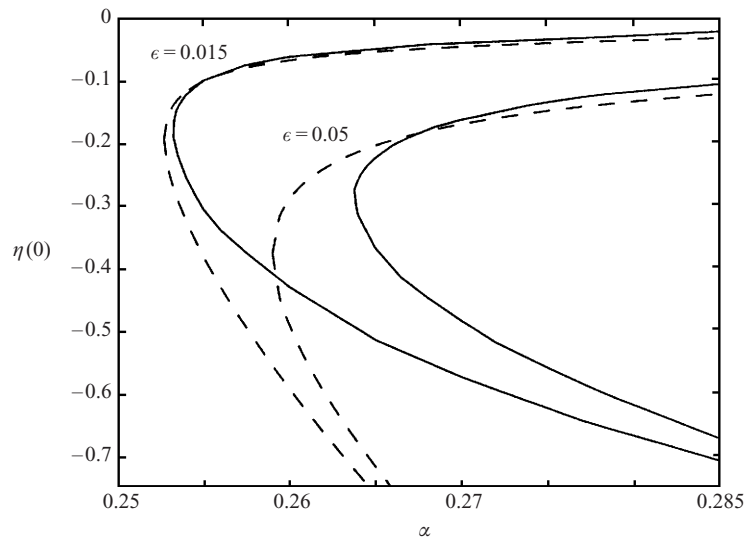


FIGURE 4. Comparison of response curves predicted by the forced NLS equation (– –) with response curves obtained by solving the water-wave equations (—).

increased. The asymptotic analysis of weakly nonlinear forced solitary waves thus confirms the results found directly using the water-wave equations and shows that the instability growth rate of forced solutions is $O(\epsilon)$ in the weakly nonlinear régime, unlike free solitary waves which feature exponentially small growth rates in this limit.

Finally, we remark in passing that all steady states with $\hat{p}_m S(0) > 0$ were found to be unstable.

5.3. Initial-value problem

Based on the stability results presented above, out of the two steady states that are possible when $\sigma > \sigma^*$, one would expect only Rayleigh's solution to be attainable. This was confirmed for the case of quiescent initial conditions, $S(X, \tau = 0) = 0$, by numerically solving the forced NLS equation (5.6) on the half domain ($X > 0$) using the semi-implicit Crank–Nicolson method described in Aranha *et al.* (1982). To avoid numerical difficulties due to impulsive start-up, the forcing was turned on within a finite time interval, imposing the boundary condition (5.9) in the form

$$S_X = \pi \hat{p}_m (1 - e^{-\tau/\tau_0}) \quad (X = 0), \quad (5.15)$$

where τ_0 is a parameter.

Numerical solutions of this initial-boundary-value problem indicate, consistent with the stability analysis, that two scenarios are possible depending on the value of σ : if $\sigma > \sigma^*$, Rayleigh's steady-state solution is approached (a decaying small-amplitude oscillation occurs about the steady state). If, on the other hand, $\sigma < \sigma^*$, so that no steady state is available, the response remains locally confined but is inherently unsteady and features large periodic fluctuations. This rather dramatic difference in the behaviour of the response is illustrated in figure 5 which shows the time histories of the response magnitude at the origin, $|S(X = 0, \tau)|$, for two values of $\sigma = 0.5$ and $\sigma = 0.06$, one above and the other below $\sigma^* = 0.1804$. In these computations, the parameter value $\tau_0 = 10$ was used. (We also carried out computations for $\tau_0 = 5$ with qualitatively very similar results.)

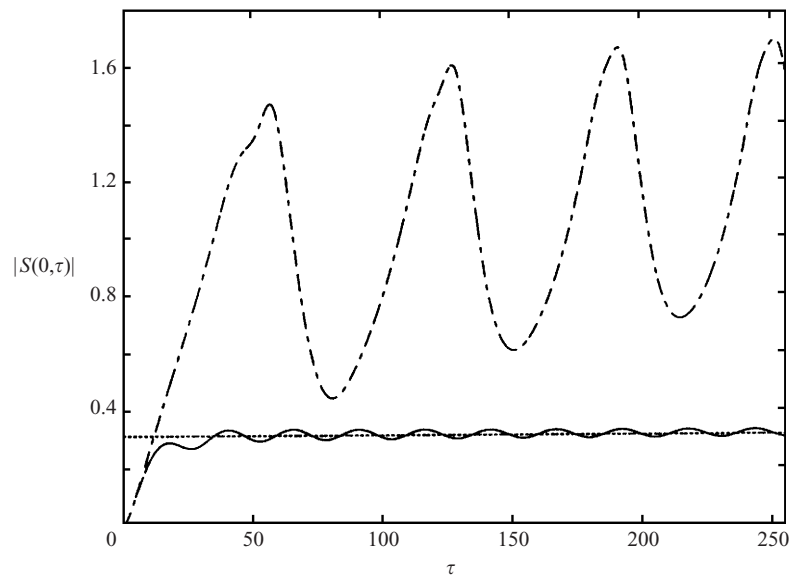


FIGURE 5. Numerical solutions of the forced NLS equation (5.6) showing time histories of the response magnitude at the origin, $|S(0, \tau)|$, for two different values of the detuning parameter σ . In the case $\sigma = 0.5 > \sigma^*$ (—), a slowly decaying oscillation about Rayleigh's theoretical steady-state amplitude (\cdots) is obtained, but in the case $\sigma = 0.06 < \sigma^*$ (---), for which no steady state is available, the response is inherently unsteady and features large-amplitude fluctuations. Results computed using $X_{\max} = 300$, $\Delta X = 0.025$ and $\Delta \tau = 2.5 \times 10^{-3}$.

Before relating these results to experimental observations, we shall discuss the role of viscous dissipation.

6. Viscous effects

The effects of viscous dissipation cannot be entirely neglected for short water waves in the gravity–capillary régime, and a steady state cannot be maintained without some type of forcing. The stability analysis of free solitary waves presented here is, therefore, most meaningful if the underlying damped wave is quasi-steady; from one instant to the next, the wave profiles agree with steady profiles obtained using potential-flow theory. This quasi-steady assumption was used by Longuet-Higgins (1997) to compute theoretical decay rates of solitary waves, in good agreement with experimental observations (Longuet-Higgins & Zhang 1997).

To assess the relative significance of viscous dissipation and check the validity of the quasi-steady assumption in our inviscid stability analysis of free solitary waves, it would be useful to make a comparison between the instability growth rates predicted by potential-flow theory in the various flow régimes and the corresponding decay rates due to dissipation: neglecting viscous effects in the stability analysis would seem justified provided the instability growth rates turn out to be much greater than the viscous decay rates. In the small-amplitude limit, for instance, the growth rates of elevation solitary waves are exponentially small and would certainly be masked by viscous effects, but this may not be the case for steep elevation or forced depression solitary waves that feature stronger instabilities.

The damping rate of a free solitary wave can be estimated following Longuet-Higgins (1997). Assuming the effects of dissipation are only moderate, the idea is

to compute the rate of external working, D , that must be done on the free surface to balance the viscous stresses there and thereby maintain a steady wave. On the assumption of weak damping, one may estimate D based on potential-flow theory and, by energy conservation, deduce the dissipation rate of a free solitary wave once the applied stresses are removed:

$$\frac{dE}{dt} = -D, \quad (6.1)$$

where E is the total energy of the wave, the sum of kinetic and potential energy.

We define the instantaneous damping rate of a solitary wave as

$$\frac{1}{\theta_{\max}} \frac{d\theta_{\max}}{dt} = \frac{1}{\theta_{\max}} \frac{d\theta_{\max}}{dE} \frac{dE}{dt}. \quad (6.2)$$

For a small-amplitude solitary wave that takes the form of a wavepacket, the right-hand side of (6.2) can be computed analytically; it turns out that the wave decays exponentially with constant damping rate twice that of a uniform train of infinitesimal waves with wavenumber equal to the carrier wavenumber of the solitary wavepacket (Longuet-Higgins 1997). For steep solitary waves, on the other hand, the right-hand side of (6.2) is no longer constant, the instantaneous damping rate now being a function of the wave steepness, and the wave decay is not exponential in general. For purposes of comparison against the corresponding instability growth rate, however, one may integrate (6.2) numerically to deduce the time evolution of θ_{\max} and then take the 'average' damping rate to be the inverse of the time required for θ_{\max} to decay by a factor of e , in analogy with the time scale of instability $1/\lambda$ which is the time over which an unstable mode grows by the same factor.

Turning next to the case of forced waves, arguing by analogy to a resonantly forced, lightly damped nonlinear oscillator, we may obtain a rough estimate of the relative significance of viscous effects by comparing the growth rate of instability against the viscous decay rate of a free depression solitary wave with the same maximum steepness as the forced response. Again, the inviscid analysis would appear justified under conditions for which the instability growth rate of the forced wave profile far exceeds the decay rate of the corresponding free solitary wave.

Figure 6 shows a comparison of the damping rates against the instability growth rates of free elevation solitary waves for a range of values of the speed parameter α . As expected, the effects of damping overwhelm those of instability in the small-amplitude limit ($\alpha \rightarrow \frac{1}{4}$) and, moreover, close to the limit point ($\alpha = 0.43$). In the intermediate range of values of α between these two extremes, corresponding to waves with maximum surface steepness θ_{\max} roughly between 7° and 25° , the growth and damping rates are of comparable magnitude, indicating that viscous effects could play a part in the stability analysis of free elevation solitary waves.

The situation can be quite different in the case of forced waves, however, depending on the strength of the forcing, as indicated in figure 7. For $\epsilon = 0.05$, corresponding to relatively weak forcing, the effects of instability are as important as viscous effects within most of the range of values of α , but for stronger forcing ($\epsilon = 0.5$) instability effects clearly begin to dominate viscous effects. As discussed below, forcing in the experiments of Longuet-Higgins & Zhang (1997) was strong, which provides justification for using inviscid stability theory to interpret the experimental observations.

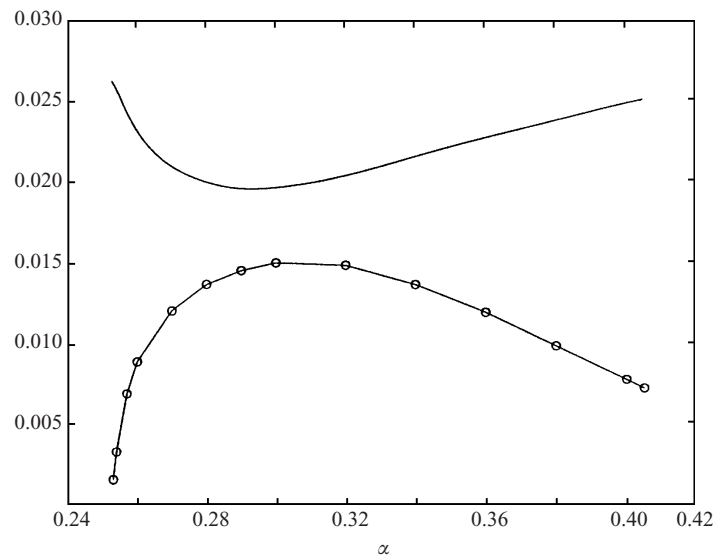


FIGURE 6. Comparison of growth rates (—○—) and damping rates (—) for free elevation solitary waves.

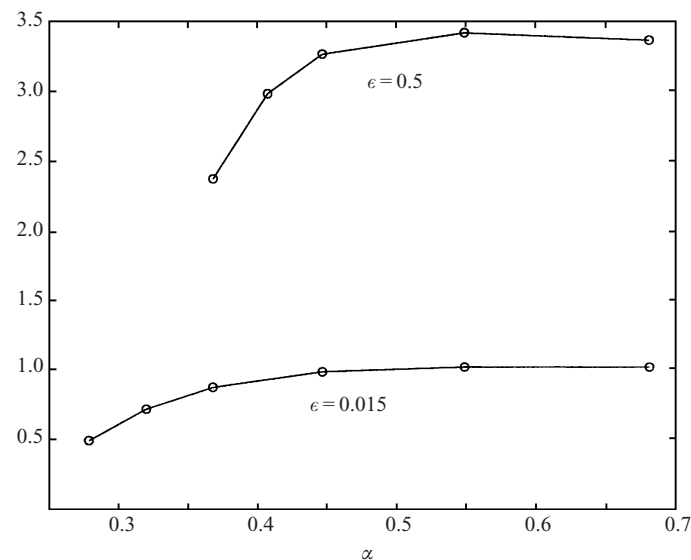


FIGURE 7. Ratio of instability growth rate of forced depression solitary wave to damping rate of free depression wave with the same maximum surface steepness.

7. Comparison with observations

One of the goals of this work was to examine the stability of the various types of free gravity–capillary solitary waves found theoretically on deep water, in order to identify those that could be observed experimentally. Our analysis focused on the two symmetric solution branches that bifurcate at the minimum gravity–capillary phase speed and confirmed that depression solitary waves with a single trough, akin

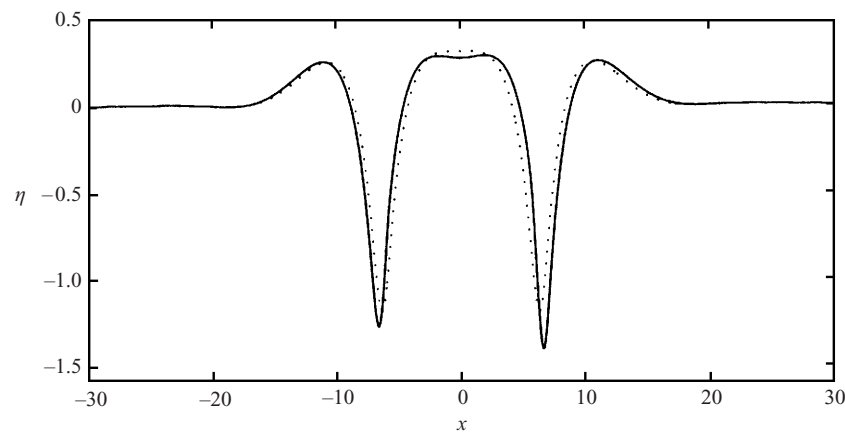


FIGURE 8. Approximate evolution of an unstable elevation wave shown at times $t = 0$ (\cdots) and $t = 2/\lambda$ ($—$). The initial state has speed parameter $\alpha = 0.38$ and corresponds to point (d) in figure 2.

to those observed by Longuet-Higgins & Zhang (1997), are indeed stable. In addition, based on our results, combinations of such single-trough profiles, like the one shown in figure 1(e), are also stable, provided that the individual pulses are sufficiently separated. We remark that Longuet-Higgins & Zhang (1997) recorded the viscous decay of single-trough free depression solitary waves and report very good agreement with theoretical predictions based on potential-flow theory taking into account dissipation (cf. (6.1) and (6.2)). This suggests that, while viscous dissipation certainly plays an important part, the combinations of single-trough solitary-wave profiles found here to be stable are likely to be observed experimentally as well.

The elevation-wave solution branch, on the other hand, was found to be unstable from the bifurcation point ($\alpha = \frac{1}{4}$) up to a critical value of α where an exchange of stabilities occurs, and it would be interesting to know the ultimate fate of an elevation-wave profile in this unstable régime. Ignoring the effects of viscous dissipation, the evolution of the instability over short times may be inferred from our analysis by adding a small amount of the unstable mode to the steady elevation-wave profile and monitoring its subsequent development over a few instability times $1/\lambda$. This procedure was carried out for the unstable elevation wave in figure 1(d) and the result is shown in figure 8. Here, the instability initially develops as a slight depression forming in the middle crest and a deepening of the right trough relative to the left trough, suggesting that this elevation wave most likely would split into two unequal depression waves that propagate at slightly different speeds. This scenario would be consistent with the behaviour of moderately steep unstable elevation solitary waves of the fifth-order KdV equation (Calvo 2000) and of a nonlinear beam equation (Chen & McKenna 1997). But, as pointed out in §6, in the case of free elevation gravity–capillary solitary waves instability effects are at most as important as viscous effects, and a definitive study of the subsequent evolution would require solving the full unsteady, viscous water-wave problem.

The theoretical findings of the present study that can be compared most directly with observations are those regarding forced depression solitary waves, and the laboratory experiments of Longuet-Higgins & Zhang (1997) are particularly relevant here. Specifically, in the light of our stability analysis of the forced response, we wish

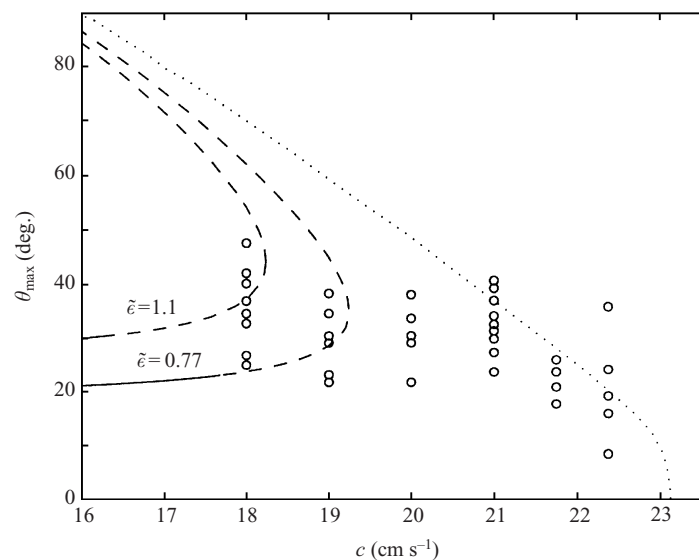


FIGURE 9. Comparison of two theoretical steady-state response curves with experimental measurements (○) reported in Longuet-Higgins & Zhang (1997). Both stable (—) and unstable segments (---) of each theoretical curve are indicated, and the solution branch of free depression solitary waves (···) is shown for reference.

to address two issues raised by these experiments: first, the fact that the experimental forced-response diagram (maximum surface steepness θ_{\max} plotted against stream speed c) did not agree closely with the theoretically predicted solution branch of free depression solitary waves as anticipated by Longuet-Higgins & Zhang (1997); and, secondly, the persistent unsteadiness of the observed forced wave profiles.

In the experiments, the stream speed c was varied while the applied pressure on the free surface was kept fixed. So, in making a comparison with the present analysis, it is convenient to use the parameter $\tilde{\epsilon} = p_{\max}/(\rho g T)^{1/2}$, rather than ϵ which involves c , to measure the strength of the applied pressure. Each value of $\tilde{\epsilon}$ then specifies a forced-response curve, analogous to those shown in figure 2, as the stream speed is varied. To determine the theoretical response curve corresponding to experimental conditions, in particular, one needs to estimate p_{\max} , the stagnation pressure of the air impinging on the free surface, based on the geometry and data given in the experiment.

The experimental set-up consists of an air chamber in sequence with a flow straightener and a converging nozzle which issues an air jet directed downward to the water surface. The air-chamber pressure (assumed to be a stagnation pressure) was reported to be always less than 3 mm of water. Based on this pressure, and the fact that loss due to the flow straightener turns out to be relatively small, it is found that $\tilde{\epsilon} = 1.1$. We note in passing that our computations confirm that this pressure amplitude creates only a small static free-surface deflection when there is no current, as reported in the experiments.

The theoretical response curve corresponding to $\tilde{\epsilon} = 1.1$ is shown in figure 9 along with a second response curve for $\tilde{\epsilon} = 0.77$, assuming a significant (30%) loss in air-chamber pressure owing to losses outside the flow straightener; the latter value of $\tilde{\epsilon}$ is adopted as a rather conservative lower bound of the forcing used in the experiments. The stable and unstable branches of the forced-response curves for $\tilde{\epsilon} = 1.1$ and

$\tilde{\epsilon} = 0.77$ according to our stability analysis are also indicated in figure 9, and the (stable) solution branch of free depression solitary waves is plotted for reference as well. It is important to note that, for the current speeds considered in the experiment, $0.77 < \tilde{\epsilon} < 1.1$ translates to values of ϵ ranging from 0.52 to 1.2. Based on our earlier estimates of the relative importance of viscous effects (see figure 7), these values of ϵ correspond to strong forcing for which inviscid stability analysis is expected to provide a reasonable approximation.

Figure 9 indicates that, for the strong forcing used in the experiment, one should not expect the solution branch corresponding to free depression solitary waves to be close to the theoretical steady-state forced response. Furthermore, it is clear from figure 9 that no stable steady states are available within the speed range considered in the experiment; as a result, one would expect the forced response to remain unsteady, which provides an explanation for the significant scatter in the maximum surface steepness recorded experimentally. This explanation is entirely consistent with the qualitative picture revealed by the forced NLS equation (see figure 5) in the weakly nonlinear régime: when no stable steady state is available, the response is locally confined but remains violently unsteady with large periodic fluctuations. It is also important to recall that, according to Longuet-Higgins & Zhang (1997), as soon as the forcing was turned off, the disturbance evolved into a free depression solitary wave that propagated in close agreement with potential-flow theory taking into account viscous dissipation. This suggests that forcing must somehow be responsible for the observed profile unsteadiness, in line with the stability analysis: as pointed out in §4.2, it is precisely the presence of forcing that causes the finite-amplitude branch of the forced-response curve to be unstable.

In the light of our findings, it would be interesting to conduct experiments for lower current speeds than those considered in Longuet-Higgins & Zhang (1997) for the purpose of confirming that steady state is reached in the speed range where Rayleigh's solution branch is found to be stable. Finally, it should be noted that the unsteadiness observed in the experiment had a three-dimensional aspect as well which may or may not be related to the two-dimensional instability discussed here.

This work was supported by the Air Force Office of Scientific Research, Air Force Materials Command, USAF, under Grant Number F49620-98-1-0388 and by the National Science Foundation Grant Number DMS-9701967. We also wish to thank the National Computational Science Alliance for a start-up allocation on the NCSA SGI/CRAY Origin 2000 machine.

Appendix. Convergence of eigenvalue computation

Here we discuss the convergence of the numerical procedure outlined in §3 for solving the stability eigenvalue problem (2.18) and (2.19).

As a preliminary check, our numerical procedure was applied to gravity solitary waves of the KdV type in water of finite depth, and the results reported in Tanaka (1986) were reproduced with the same precision and convergence behaviour. Attention was then focused on the gravity–capillary problem of interest here, and a typical example of convergence for an unstable forced depression wave is shown in table 3. In the case of free elevation solitary waves, computations tended to be more expensive as indicated by the example of convergence shown in table 4 for a free elevation wave with $\alpha = 0.30$. The corresponding instability mode shape is displayed in figure 10.

A computational detail, not fully discussed in Tanaka (1986), is the implementation

$\beta = 0.1$		$\beta = 0.05$	
$\Delta\gamma$	λ	$\Delta\gamma$	λ
2.5×10^{-2}	0.025	2.5×10^{-2}	0.025
1.3×10^{-2}	0.026	1.3×10^{-2}	0.026
6.3×10^{-3}	0.027	6.3×10^{-3}	0.027
3.1×10^{-3}	0.027	3.1×10^{-3}	0.027

TABLE 3. Eigenvalue convergence for an unstable forced depression wave ($\alpha = 0.368$ and $\epsilon = 0.05$) as $\Delta\gamma$ and β are varied. The domain size is $\Phi_{\max} = 85$ ($\gamma_{\max} = 4.4$) and $m = 3$.

$\Phi_{\max} = 65$		$\Phi_{\max} = 90$	
$\Delta\Phi$	λ	$\Delta\Phi$	λ
0.10	0.0138	0.10	0.0139
0.05	0.0150	0.05	0.0150
0.025	0.0153	0.025	0.0153
0.015	0.0153	0.015	0.0153

TABLE 4. Eigenvalue convergence for an unstable elevation wave ($\alpha = 0.30$) as $\Delta\Phi$ and Φ_{\max} are varied.

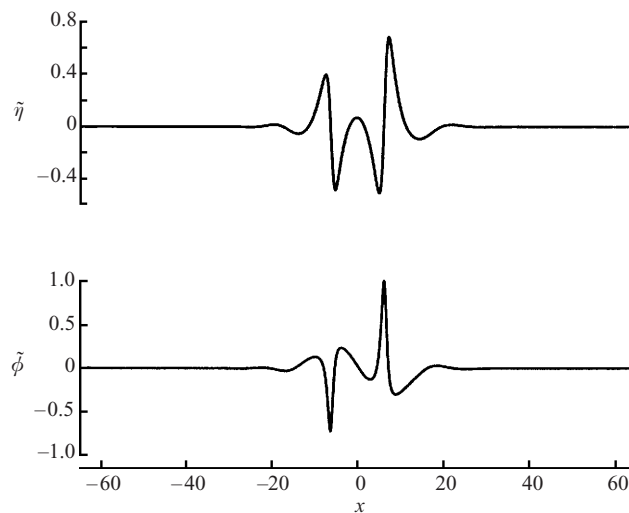


FIGURE 10. Instability mode shape for elevation wave with $\alpha = 0.30$.

of homogeneous boundary conditions at the ends of the domain. In evaluating derivatives there, a finite-difference stencil was used that took into account ‘ghost’ points lying directly outside the domain where the mode-shape values are imposed to be zero. Varying the number of ghost points used had no significant impact on the computed eigenvalues and mode shapes.

REFERENCES

- AKYLAS, T. R. 1984 On the excitation of nonlinear water waves by a moving pressure distribution oscillating at resonant frequency. *Phys. Fluids* **27**, 2803–2807.

- AKYLAS, T. R. 1993 Envelope solitons with stationary crests. *Phys. Fluids A* **5**, 789–791.
- AKYLAS, T. R., DIAS, F. & GRIMSHAW, R. H. J. 1998 The effect of the induced mean flow on solitary waves in deep water. *J. Fluid Mech.* **355**, 317–328.
- ARANHA, J. A., YUE, D. K. P. & MEI, C. C. 1982 Nonlinear waves near a cut-off frequency in an acoustic duct—a numerical study. *J. Fluid Mech.* **121**, 465–485.
- BARNARD, B. J. S., MAHONY, J. J. & PRITCHARD, W. G. 1977 The excitation of surface waves near a cut-off frequency. *Phil. Trans. R. Soc. Lond.* **286**, 87–123.
- BUFFONI, B., CHAMPNEYS, A. R. & TOLAND, J. F. 1995 Bifurcation and coalescence of a plethora of homoclinic orbits for a Hamiltonian system. *J. Dyn. Diff. Equat.* **8**, 221–281.
- BURYAK, A. V. & CHAMPNEYS, A. R. 1997 On the stability of solitary wave solutions of the fifth-order KdV equation. *Phys. Lett. A* **233**, 58–62.
- CALVO, D. C. 2000 Dynamics and stability of gravity–capillary solitary waves. PhD Thesis, Massachusetts Institute of Technology.
- CALVO, D. C., YANG, T.-S. & AKYLAS, T. R. 2000 On the stability of solitary waves with decaying oscillatory tails. *Proc. R. Soc. Lond. A* **456**, 469–487.
- CHEN, Y. & MCKENNA, P. J. 1997 Travelling waves in a nonlinearly suspended beam: some computational results and four open questions. *Phil. Trans. R. Soc. Lond. A* **355**, 2175–2184.
- DIAS, F. & KUZNETSOV, E. A. 1999 On the nonlinear stability of solitary wave solutions of the fifth-order Korteweg–de Vries equation. *Phys. Lett. A* **263**, 98–104.
- DIAS, F., MENASCE, D. & VANDEN-BROECK, J.-M. 1996 Numerical study of capillary–gravity solitary waves. *Eur. J. Mech. B* **15**, 17–36.
- FEDOROV, A. V. & MELVILLE, W. K. 1998 Nonlinear gravity–capillary waves with forcing and dissipation. *J. Fluid Mech.* **354**, 1–42.
- LONGUET-HIGGINS, M. S. 1989 Capillary–gravity waves of solitary type on deep water. *J. Fluid Mech.* **200**, 451–470.
- LONGUET-HIGGINS, M. S. 1993 Capillary–gravity waves of solitary type and envelope solitons on deep water. *J. Fluid Mech.* **252**, 703–711.
- LONGUET-HIGGINS, M. S. 1995 Parasitic capillary waves: a direct calculation. *J. Fluid Mech.* **301**, 79–107.
- LONGUET-HIGGINS, M. S. 1997 Viscous dissipation in steep capillary–gravity waves. *J. Fluid Mech.* **344**, 271–289.
- LONGUET-HIGGINS, M. S. & ZHANG, X. 1997 Experiments on capillary–gravity waves of solitary type on deep water. *Phys. Fluids* **9**, 1963–1968.
- MALOMED, B. & VANDEN-BROECK, J.-M. 1996 Solitary wave interactions for the fifth-order KdV equation. *Contemp. Maths* **200**, 133–143.
- PĂRĂU, E. & DIAS, F. 2000 Ondes solitaires forcées de capillarité-gravité. *C. R. Acad. Sci. Paris I* **331**, 655–660.
- PERLIN, M., LIN, H. & TING, C.-L. 1993 On parasitic capillary waves generated by steep gravity waves: an experimental investigation with spatial and temporal measurements. *J. Fluid Mech.* **255**, 597–620.
- TANAKA, M. 1986 The stability of solitary waves. *Phys. Fluids* **29**, 650–655.
- VANDEN-BROECK, J.-M. & DIAS, F. 1992 Gravity–capillary solitary waves in water of infinite depth and related free-surface flows. *J. Fluid Mech.* **240**, 549–557.
- WHITHAM, G. B. 1974 *Linear and Nonlinear Waves*. Wiley-Interscience.
- YANG, T.-S. & AKYLAS, T. R. 1997 On asymmetric gravity–capillary solitary waves. *J. Fluid Mech.* **330**, 215–232.
- ZHANG, X. 1995 Capillary–gravity and capillary waves generated in a wind wave tank: observations and theories. *J. Fluid Mech.* **289**, 51–82.
- ZHANG, X. 1999 Observations on waveforms of capillary and gravity–capillary waves. *Eur. J. Mech. B* **18**, 373–388.
- ZUFIRIA, J. A. 1987 Symmetry breaking in periodic and solitary gravity–capillary waves on water of finite depth. *J. Fluid Mech.* **184**, 183–206.